JGR Solid Earth

RESEARCH ARTICLE
10.1029/2024JB029104

Strong Lg-Wave Attenuation Reveals Quarter-Toroidal Crustal Melting Around the Yakutat Terrane in South-Central Alaska

Geng Yang[1,2], Lian-Feng Zhao[1,3], Xiao-Bi Xie[4], Xi He[1], Lei Zhang[5], and Zhen-Xing Yao[1]

[1]Key Laboratory of Earth and Planetary Physics, Institute of Geology and Geophysics, Chinese Academy of Sciences, Beijing, China, [2]College of Earth and Planetary Sciences, University of Chinese Academy of Sciences, Beijing, China, [3]Heilongjiang Mohe Observatory of Geophysics, Institute of Geology and Geophysics, Chinese Academy of Sciences, Beijing, China, [4]Institute of Geophysics and Planetary Physics, University of California at Santa Cruz, Santa Cruz, CA, USA, [5]School of Earth and Space Sciences, Peking University, Beijing, China

Abstract South-central Alaska features a history of massive volcanic activity. How the Denali volcanic gap (DVG) formed and why the Wrangell volcanoes are clustered remain vigorously debated. Investigating the crustal thermal structure can be crucial for understanding subsurface magmatic activity. We present a high-resolution broadband Lg-wave attenuation model to constrain crustal thermal anomalies beneath Alaska. Strong Lg attenuation is observed beneath the volcanoes in south-central Alaska, indicating thermal anomalies and possible melting in the crust. In contrast, the central Yakutat terrane (YT) and DVG are characterized by weak Lg attenuation, suggesting the existence of a cool crust that prevents hot mantle materials from invading the crust. This cool crust is likely the reason for the DVG. Quarter-toroidal crustal melting with strong attenuation is revealed around the YT. This curved zone of crustal melting, possibly driven by toroidal mantle flow, weakly connects the Wrangell and Buzzard Creek-Jumbo Dome magmatic chambers.

Plain Language Summary The Alaskan mainland is located at the western end of the North American plate. This region is adjacent to the Bering Sea to the west and overlies the subducting Pacific Plate to the south. The Yakutat microplate subducts northward below Alaska with a velocity similar to that of the Pacific plate but with a lower angle. Many volcanoes have developed in south-central Alaska, including those in the Aleutian arc, the Buzzard Creek-Jumbo Dome, and the Wrangell volcanic field (WVF). However, the origins, storage and transport patterns of the magmas feeding these volcanoes are still unclear and under debate. In this study, we conduct Lg-wave attenuation tomography on the Alaskan mainland and use the results to investigate the regional crustal thermal structure. The imaging results reveal a cold Yakutat terrane and hot crustal features beneath the volcanoes. The Denali volcanic gap is characterized by weak crustal attenuation, indicating that cool crust may have inhibited volcanic activity. Quarter-toroidal crustal melting is revealed by a curved belt of strong attenuation. The crustal magmatic chambers may weakly connect the WVF and the Buzzard Creek-Jumbo Dome volcanoes.

Key Points:

- A high-resolution broadband Lg-wave attenuation model is obtained for the Alaskan mainland
- Strong Lg-wave attenuation beneath the volcanoes indicates crustal thermal anomalies and melting
- A quarter-toroidal crustal melting belt weakly connects the magmatic chambers beneath the Buzzard Creek-Jumbo Dome and Wrangell volcanoes

Supporting Information:

Supporting Information may be found in the online version of this article.

Correspondence to:

L.-F. Zhao,
zhaolf@mail.iggcas.ac.cn

Citation:

Yang, G., Zhao, L.-F., Xie, X.-B., He, X., Zhang, L., & Yao, Z.-X. (2024). Strong Lg-wave attenuation reveals quarter-toroidal crustal melting around the Yakutat terrane in south-central Alaska. *Journal of Geophysical Research: Solid Earth*, *129*, e2024JB029104. https://doi.org/10.1029/2024JB029104

Received 13 MAR 2024
Accepted 25 AUG 2024

Author Contributions:

Conceptualization: Geng Yang, Lian-Feng Zhao
Data curation: Geng Yang, Lei Zhang
Formal analysis: Geng Yang, Xi He
Funding acquisition: Lian-Feng Zhao, Zhen-Xing Yao
Investigation: Geng Yang
Methodology: Geng Yang, Lian-Feng Zhao, Xiao-Bi Xie
Project administration: Lian-Feng Zhao, Zhen-Xing Yao
Software: Geng Yang, Lian-Feng Zhao, Xi He, Lei Zhang
Supervision: Lian-Feng Zhao, Xiao-Bi Xie, Zhen-Xing Yao
Validation: Geng Yang
Writing – original draft: Geng Yang
Writing – review & editing: Lian-Feng Zhao, Xiao-Bi Xie, Xi He, Lei Zhang

1. Introduction

The Alaskan mainland overlies the subducting Pacific plate and Yakutat microplate as they subduct beneath the southern margin of the North American plate (Figure 1a). As an accreted section of an oceanic plateau, the Yakutat terrane (YT) originated from the Kula–Farallon spreading ridge at approximately 50 Ma, migrated northward along the Queen Charlotte-Fairweather fault system, and formed flat-slab subduction with clear Wadati–Benioff Zone seismicity (Chuang et al., 2017; Daly et al., 2021; Davis & Plafker, 1986; Eberhart-Phillips et al., 2006; Plafker et al., 1994). The Yakutat and Pacific plates move in similar directions and at similar velocities (Elliott et al., 2010; Leonard et al., 2007). Complex plate coupling has introduced intense intraplate deformation, abundant seismicity, active surface volcanism, and complex subsurface magma storage and transport patterns.

South-central Alaska features massive volcanoes of different types, including intraplate volcanoes, Aleutian arc volcanoes, and a group of densely clustered volcanoes called the Wrangell volcanic field (WVF). Volcanoes are distributed along the Aleutian arc, starting from the western Aleutians and extending eastward to Alaska, but are absent within an ~400 km wide zone known as the Denali volcanic gap (DVG) in south-central Alaska. On the far

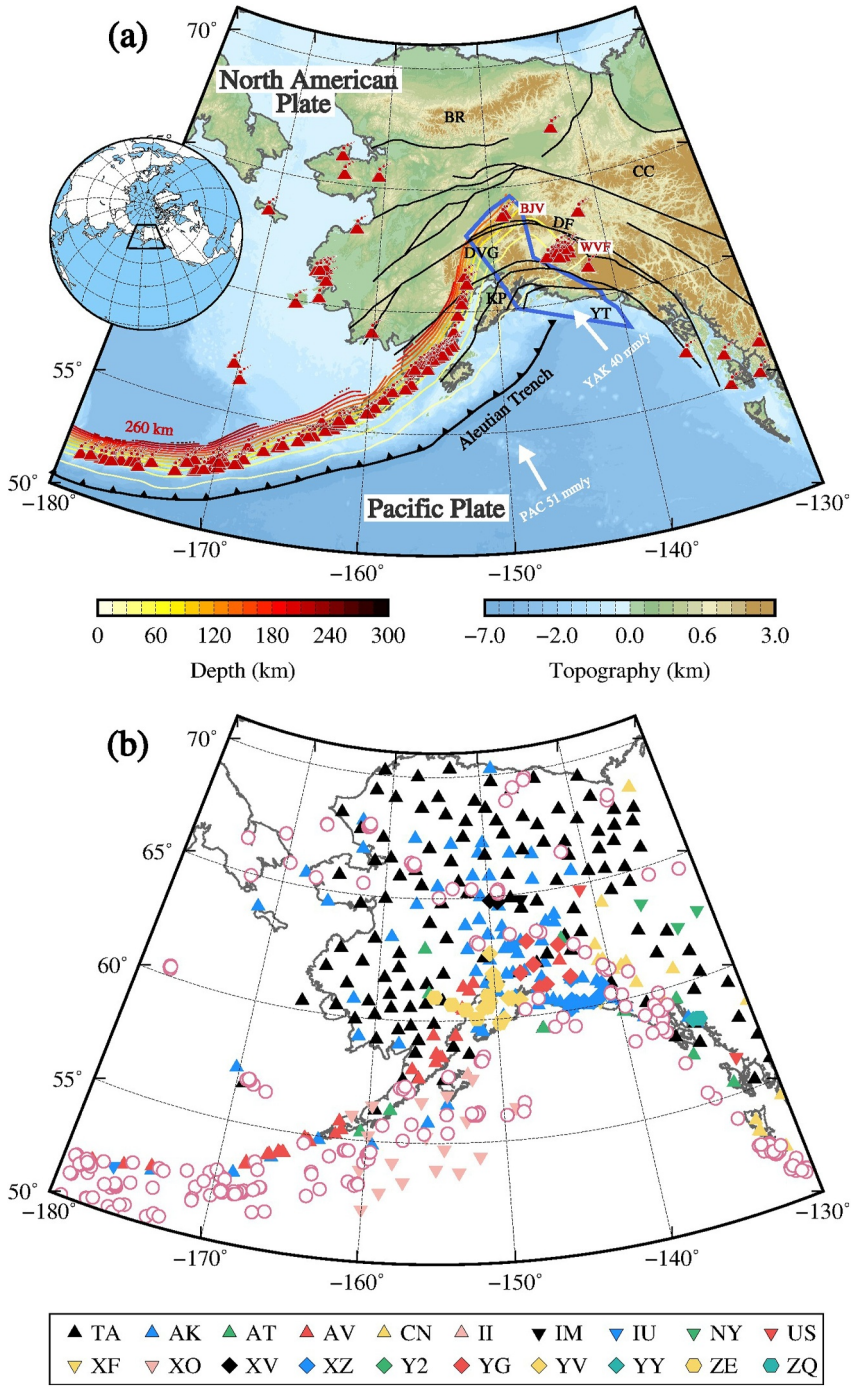

Figure 1. (a) Regional tectonic setting. The black lines are major fault systems (Koehler, 2013; Wilson et al., 2015). The red triangles denote locations of volcanoes in Alaska younger than 2 million years (Cameron & Crass, 2022). The Slab 2.0 model provided the depth isobaths (with an interval of 20 km) of the subducting Pacific slab (Hayes et al., 2018). The location of the Yakutat Terrane is bounded by the blue polygon (Eberhart-Phillips et al., 2006). The white vectors indicate the motion velocities and directions of the Pacific and Yakutat plates (Elliott et al., 2010; Leonard et al., 2007). BR: Brooks Range, BJV: Buzzard Creek-Jumbo Dome volcanoes, CC: Canadian Cordillera, DF: Denali Fault, DVG: Denali volcanic gap, KP: Kenai Peninsula, PAC: Pacific Plate, WVF: Wrangell Volcanic Field, YAK: Yakutat Plate, YT: Yakutat Terrane. (b) Map showing the locations of the stations (triangles, diamonds, and pentagons) and earthquakes (circles) used in this study. Network names are indicated at the bottom of the figure, and their information is listed in Tables S1 and S2 in Supporting Information S2.

side of the gap, the Buzzard Creek-Jumbo Dome volcanoes (BJV) developed at ~147° W (Figure 1a). The abrupt absence of volcanic activity in the DVG remains poorly explained due to the ambiguous lithospheric structures there. The wedge-shaped Yakutat plate is subducting under the DVG at a relatively low angle, which may have cooled the mantle wedge and hindered the hot asthenosphere from promoting volcanism (e.g., Abers, 2008; Christeson et al., 2010; Chuang et al., 2017; Finzel et al., 2011; Martin-Short et al., 2018). However, previous studies have failed to reach a consensus regarding the exact velocity structures beneath the DVG. For example, a high-velocity upper mantle has been observed beneath the DVG (Jiang et al., 2018; Liang et al., 2024; Ward & Lin, 2018; Yang & Gao, 2020), suggesting that molten magmatic materials do not exist. In contrast, some tomographic results revealed low-velocity anomalies in the mantle wedge beneath the volcanic gap (Feng & Ritzwoller, 2019; Gou et al., 2019; Martin-Short et al., 2018), leading to the opposite conclusion that hot magma may have been generated but has not yet been transported to the surface to form volcanism. The question arises as to whether magmatic material exists in the crust under the DVG. It is necessary to provide additional data to further investigate the differences between regions with and without active volcanism.

On the eastern edge of the Yakutat plate, the WVF extends northwestward for approximately 500 km, from Canada to south-central Alaska, and is composed of large andesitic shield volcanoes and voluminous calc-alkaline volcanic rocks (Preece & Hart, 2004; Richter et al., 1990). The formation of the WVF is under ongoing debate. Although the WVF is generally characterized by continental arc volcanism, geochemical evidence of adakites suggests the occurrence of slab-edge melting and asthenospheric upwelling related to Yakutat subduction (Brueseke et al., 2019; He & Lü, 2021; Martin-Short et al., 2018; Preece & Hart, 2004). The Wrangell magmatism may have originated from melted mantle materials carried by potential toroidal mantle flow around the slab edge, as supported by numerical simulations (Jadamec & Billen, 2010) and seismic anisotropy observations (Christensen & Abers, 2010; Feng et al., 2020; Hanna & Long, 2012; McPherson et al., 2020; Venereau et al., 2019). A controversial high-velocity slab fragment called the Wrangell slab has been suggested to exist beneath the WVF and represents another possible magmatic origin of the WVF (Daly et al., 2021; Estève et al., 2021; Gou et al., 2019; Jiang et al., 2018; Yang & Gao, 2020). Thus, detailed documentation of the crustal thermal structure could provide new constraints on the development of Wrangell volcanism.

Seismic attenuation, or the quality factor Q, usually provides good constraints on the viscoelastic structure and is sensitive to thermodynamic processes in the lithosphere, such as partial melting and high-temperature magmatism (Boyd et al., 2004; Dalton et al., 2009; Debayle et al., 2020). Several seismic attenuation studies have been conducted for this region (e.g., Hearn, 2021; Mahanama & Cramer, 2023; McNamara, 2000; McSweeney et al., 1991; Soto Castaneda et al., 2021; Stachnik et al., 2004). However, limitations of resolution and certain differences between these results make it challenging to achieve a unified understanding for the aforementioned issues. Regional Lg-waves propagating in the continental crust waveguide are an ideal phase for investigating crustal attenuation. In this study, based on vertical-component waveform data recorded by 20 permanent and temporary seismic networks in Alaska, we established a broadband crustal Lg-wave attenuation model for Alaska and nearby regions. By linking the observed low-Q_{Lg} anomalies with surface volcanic activity and deep magmatic origins and transport, we attempt to explain the formation of the DVG and WVF and their relationships with the Yakutat subduction system.

2. Data and Methods

2.1. Regional Waveform Data

This study utilized 397 permanent and temporary stations deployed across Alaska and northwestern Canada (Figure 1b). We selected waveforms from 242 crustal earthquakes that occurred between January 2000 and July 2021 with known focal mechanisms in the Harvard Centroid Moment Tensor Catalog (CMT) (Ekstrom et al., 2012). The magnitudes of the earthquakes were within $4.3 \leq m_b \leq 6.5$, and the epicentral distances varied from 200 to 2,000 km. Detailed station and earthquake information is listed in Tables S1–S3 in Supporting Information S2.

2.2. Lg-Wave Spectral Amplitude

The Lg-wave spectral amplitude can be calculated following Zhao et al. (2013). As illustrated in Figure 2a, in a regional seismic record, the Lg-wave is usually the most prominent phase and carries the most energy around 1.0 Hz. The energy distribution in the arrival time-frequency domain is illustrated in a displacement spectrogram,

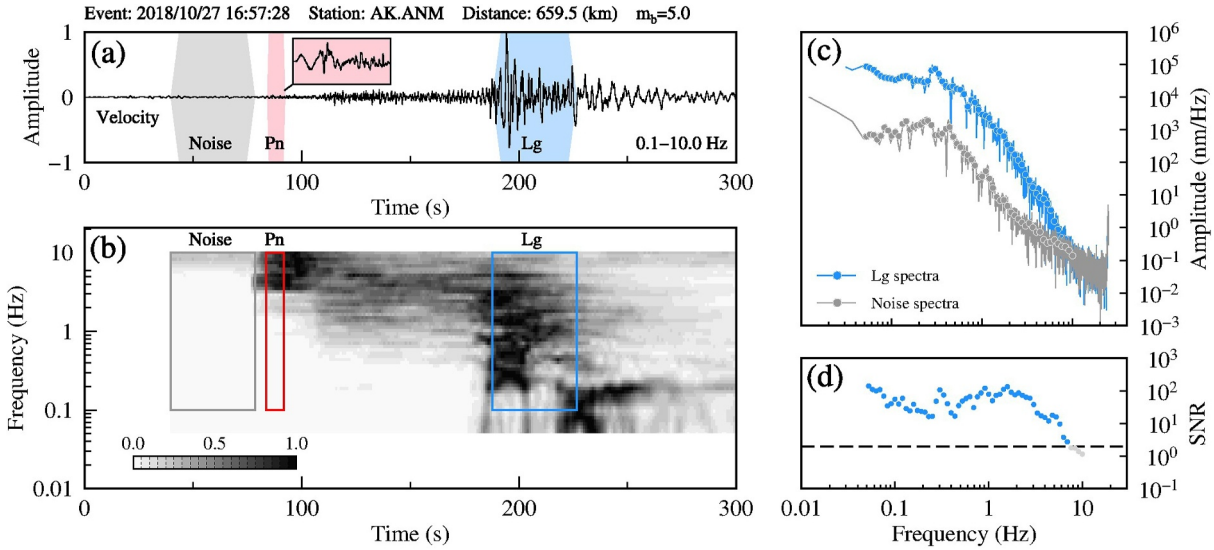

Figure 2. Spectral amplitude measurement of the Lg-wave. (a) Velocity seismogram from a regional event that occurred on 27 October 2018, recorded at station AK.ANM. The gray, red, and blue time windows sample the pre-event noise, Pn signal, and Lg signal, respectively. (b) Time-frequency displacement spectrogram of the sample seismogram. (c) Spectra of Lg and pre-event noise. (d) Signal-to-noise ratio (SNR). Lg data with an SNR <2.0 are discarded and represented by gray dots.

which is calculated using a 20-s windowed Fourier transform moving at a 2-s time step (Figure 2b). The Pn energy is mainly distributed at 2.0–10.0 Hz, and the Lg energy is dominant between 0.2 and 8.0 Hz. The pre-event noise is usually very weak compared to that of the regional phases. Figure S1 in Supporting Information S1 shows a profile recorded from an earthquake that occurred on 27 October 2018, and the Lg signals are shown in the figure. Based on the spectrogram, we use a 0.6 km/s-long group velocity window to locate the Lg signal. By scanning the waveforms using a sampling window between 3.7 and 2.9 km/s, the section of the waveform with the maximum energy is identified as the Lg signal (Yang et al., 2023; Zhao et al., 2013). The spectral amplitudes of the Lg-wave and pre-event noise series were calculated using the fast Fourier transform (Figure 2c). The signal-to-noise ratio (SNR) was calculated by $A_{obs}(f)/A_{noise}(f)$ at each frequency. We used an SNR >2.0 as the threshold for data quality control, and data points below this threshold were excluded (Figure 2d). Finally, the equation $A^2(f) = A^2_{obs}(f) - A^2_{noise}(f)$ was used to remove the noise effect and obtain the Lg-wave spectral amplitudes for inversion (Ringdal et al., 1992).

The spectral amplitude of the Lg-wave can be expressed as (Xie, 1993)

$$A_{ki}(f) = S_k(f) \cdot G_{ki}(\Delta, f) \cdot \Gamma_{ki}(\Delta, f) \cdot P_i(f) \cdot r_{ki}(f), \quad (1)$$

where $A(f)$ is the displacement spectral amplitude recorded at station i from event k, f is the frequency, $S(f)$ is the source spectrum, $G(\Delta, f)$ is the geometrical spreading factor, $\Gamma(\Delta, f)$ is the attenuation term, $P(f)$ is the site response and $r(f)$ is the random error in the data. The Brune displacement source term $S(f)$ can be further expressed as $S(f) = M_0/4\pi\rho\beta^3 \cdot \left[1 + \frac{f^2}{f_c^2}\right]^{-1}$ (Sereno et al., 1988), where M_0 represents the seismic moment; ρ is the density, with a value 2.7 g/cm^3 used for the crust; β is the average crustal shear-wave velocity, with a value of 3.5 km/s for Alaska (Berg et al., 2020); and f_c is the corner frequency. The geometrical spreading is $G = (\Delta_0\Delta)^{-1/2}$, with Δ representing the epicentral distance and Δ_0 representing a reference distance fixed at 100 km (Pasyanos et al., 2009; Street et al., 1975; Zhao et al., 2013). The attenuation term $\Gamma(\Delta, f)$ can be expressed as $\Gamma(\Delta, f) = exp\left[-\frac{\pi f}{\beta}B(\Delta, f)\right]$, where $B(\Delta, f) = \int_{ray}\frac{ds}{Q(f)}$ is an integral over the great circle raypath. If an event is recorded by two stations i and j within a small azimuth range (<15°), a two-station spectral ratio can be calculated

$$\frac{A_i}{A_j} = \left(\frac{\Delta_i}{\Delta_j}\right)^{-\frac{1}{2}} \Gamma_{ij} \left(\frac{P_i}{P_j}\right) = \left(\frac{\Delta_i}{\Delta_j}\right)^{-\frac{1}{2}} \cdot \exp\left[\frac{-\pi f}{\beta} \int_j^i \frac{ds}{Q(\mathrm{x}, \mathrm{y}, f)}\right], \tag{2}$$

where Γ_{ij} represents the contribution of attenuation over the great circle between stations i and j.

2.3. Q_{Lg} Inversion

Single-station amplitude data can provide dense raypath coverage, while two-station amplitude ratio data can reduce the tradeoff between the source and attenuation. Combining both can improve the resolution and confidence of the inversion result. We linearize Equations 1 and 2 in the logarithmic domain to establish the single- and two-station inversion systems. For the single-station data set, applying the natural logarithm to Equation 1, we have

$$\ln[A(f)] - \ln[G(\Delta, f)] = \ln[S(f)] - \frac{\pi f}{\beta} B(\Delta, f), \tag{3}$$

where the site and random terms are neglected. The attenuation and source function can be further separated into a background part and the perturbation

$$\frac{1}{Q(x, y, f)} \approx \frac{1}{Q^0(x, y, f)} - \frac{\delta Q(x, y, f)}{\left[Q^0(x, y, f)\right]^2}, \tag{4}$$

and

$$\ln[S(f)] = \ln\left[S^0(f)\right] + \delta \ln[S(f)]. \tag{5}$$

Therefore, Equation 3 can be further expressed as

$$\ln[A(f)] - \ln[G(\Delta, f)] - \ln\left[S^0(f)\right] + \frac{\pi f}{\beta} B^0(\Delta, f) = \delta \ln[S(f)] - \frac{\pi f}{\beta} \delta B(\Delta, f), \tag{6}$$

where variables with superscript 0 denote their values in the initial model or the intermediate model between iterations, δB is the perturbation of the attenuation term $B(\Delta, f)$, $\delta \ln[S(f)]$ is the perturbation of the logarithmic Lg-wave source function, and

$$\delta B(\Delta, f) = \sum_{g=1}^{G} \int_g \frac{\delta Q(x, y, f)}{\left[Q^0(x, y, f)\right]^2} ds, \tag{7}$$

where g and G represent the grid number and the total number of grids along the raypath, respectively. The integral in Equation 7 was calculated using the bilinear function in each inversion cell

$$Q(x, y) = \sum_{p=1}^{4} a_p w_p(x, y), \tag{8}$$

where $w_1 = 1$, $w_2 = x$, $w_3 = y$, $w_4 = xy$, and a_p are the interpolation parameters obtained from Q_{Lg} values. For multiple sources and stations, we combine Equations 6 and 7 into a linear system:

$$\boldsymbol{H_s} = \boldsymbol{A_s} \cdot \delta \boldsymbol{Q} + \boldsymbol{E} \cdot \delta \boldsymbol{S}, \tag{9}$$

where $\boldsymbol{H_s}$ is a vector composed of residuals between the observed and synthetic Lg spectra and $\delta \boldsymbol{Q}$ and $\delta \boldsymbol{S}$ are the perturbations of Q_{Lg} and the source term, respectively. Its elements are as follows:

$$h_j = \ln[A_j(f)] - \left[\ln[G_j(\Delta, f)] + \ln\left[S_k^0(f)\right] - \frac{\pi f}{\beta} B_j^0(\Delta, f)\right], \tag{10}$$

where h_j is the residual between the observed logarithmic Lg spectral amplitude $\ln[A_j(f)]$ recorded at station i, and synthetic Lg spectra $\left[\ln[G_j(\Delta, f)] + \ln\left[S_k^0(f)\right] - \frac{\pi f}{\beta} B_j^0(\Delta, f)\right]$, composed of the attenuation term $B(\Delta, f)$, source term $S(f)$ and geometrical spreading term $G(\Delta, f)$. The inversion is conducted by minimize the h_j. The matrices $\boldsymbol{A_s}$ and $\boldsymbol{E}$ establish the relationships between $\delta\boldsymbol{Q}$ and $\boldsymbol{H_s}$ and between $\delta\boldsymbol{S}$ and $\boldsymbol{H_s}$, respectively. Similarly, we can create a linear system for the two-station data set

$$\boldsymbol{H_t} = \boldsymbol{A_t} \cdot \delta\boldsymbol{Q}, \tag{11}$$

where $\boldsymbol{H_t}$ is a vector composed of residuals between the observed and synthetic spectral ratios and the matrix $\boldsymbol{A_t}$ can be obtained by discretizing Equation 2. The related residual between the observed and synthetic Lg spectra ratio can be further expressed as

$$h_{ij} = \ln[A_i(f)] - \ln[A_j(f)] - \left[\ln[G_{ki}(\Delta, f)] - \ln[G_{kj}(\Delta, f)] - \frac{\pi f}{\beta}\int_j^i \frac{ds}{Q(\mathrm{x,y},f)}\right], \tag{12}$$

where $\ln[A_i(f)]$–$\ln[A_j(f)]$ is the observed logarithmic spectral amplitude ratio between stations i and j, and $\left[\ln[G_{ki}(\Delta, f)] - \ln[G_{kj}(\Delta, f)] - \frac{\pi f}{\beta}\int_j^i \frac{ds}{Q(\mathrm{x,y},f)}\right]$ is the synthetic Lg spectra ratio. Combining Equations 9 and 11, we obtain a joint tomography equation

$$\begin{bmatrix}\boldsymbol{H_s}\\ \boldsymbol{H_t}\end{bmatrix} = \begin{bmatrix}\boldsymbol{A_s}\\ \boldsymbol{A_t}\end{bmatrix} \cdot \delta\boldsymbol{Q} + \begin{bmatrix}\boldsymbol{E}\\ 0\end{bmatrix} \cdot \delta\boldsymbol{S}. \tag{13}$$

To solve the inverse problem, an iterative inversion method was adopted. Single- and two-station data are jointly solved by the least squares orthogonal factorization (LSQR) inversion method (Paige & Saunders, 1982) at each frequency independently. The residual vector between the observed and synthetic spectral amplitudes, $\boldsymbol{b} = \begin{bmatrix}\boldsymbol{H_s}\\ \boldsymbol{H_t}\end{bmatrix}$, can be obtained to solve the model modification vector, $\boldsymbol{m} = \begin{bmatrix}\delta\boldsymbol{Q}\\ \delta\boldsymbol{S}\end{bmatrix}$. A coefficient matrix, $\boldsymbol{A} = \begin{bmatrix}\boldsymbol{A_s} & \boldsymbol{E}\\ \boldsymbol{A_t} & 0\end{bmatrix}$, can be used to simplify Equation 13 as:

$$\boldsymbol{Am} = \boldsymbol{b}. \tag{14}$$

During each iteration, δQ remains small, while Q^0 is iteratively updated until the rms residual of the amplitude becomes stable (Figures S2 and S3 in Supporting Information S1). The inversion starts from a unit source function, and a constant initial Q_{Lg} model obtained by linear regression of the interstation data (Figure S4 in Supporting Information S1) (Zhao et al., 2013). During the inversion, a damping parameter λ is used for regularization by minimizing the following:

$$\left\| \begin{bmatrix}\boldsymbol{A}\\ \lambda\boldsymbol{I}\end{bmatrix}\boldsymbol{m} - \begin{bmatrix}\boldsymbol{b}\\ 0\end{bmatrix} \right\|_2, \tag{15}$$

where $\boldsymbol{I}$ is an identity matrix. We determined the damping parameter λ by considering the tradeoff between variance reduction and the model norm. Based on the simplified inversion matrix equation $\boldsymbol{Am} = \boldsymbol{b}$, the L-curve was obtained using the residual norm $\|\boldsymbol{Am} - \boldsymbol{b}\|_2$ versus the model norm $\|\boldsymbol{m}\|_2$ with different damping parameters (Figure S5 in Supporting Information S1). Smaller damping values were used in subsequent iterations to ensure a better data fit while preserving robust anomaly features. During each iteration, we also applied first-order linear

smoothness constraints to the solution along the longitudinal and latitudinal directions (e.g., Zhao et al., 2010). Based on the iterative use of Equation 13, the inverted source functions, seismic moment, and corner frequency for each event are shown in Figure S6 and Table S3 in Supporting Information S1 and S2. During the inversion, we assumed the sum of the perturbations of site responses (in logarithmic form) $\sum_{i=1}^{N} \delta \ln P_i = 0$ and simultaneously controlled the relative variation in site responses during the inversion. We then pushed the unsolved postinversion residuals into the site term (Ottemöller et al., 2002; Zhao & Mousavi, 2018). That is, the site response for each station was finally determined based on both the obtained source and attenuation terms (Figure S7 in Supporting Information S1). Compared to the initial model, the data residuals after the inversion are close to the unbiased normal distribution, and the root mean square (rms) of the data are significantly reduced (Figure S8 in Supporting Information S1).

3. Results

Crustal Lg-wave attenuation models were obtained at 58 individual frequencies between 0.01 and 10.0 Hz. The lateral variations in Q_{Lg} correlated well with regional tectonics at individual frequencies. Figures 3a–3c show examples of Q_{Lg} maps at 0.5, 1.0, and 2.0 Hz, respectively. In most areas of the mainland with dense raypath coverage, the resulting resolution reaches 1.0° × 1.0° at most frequencies (Figures 3e–3f and Figures S9 and S10 in Supporting Information S1). Overall, the Q_{Lg} values exhibit similar frequency dependencies in the study region (Figure 4), including the Arctic Alaska Terrane (AAT), the Ocean Domain Terranes (ODT), Central Alaska (CA), the Yukon Composite Terrane (YCT), and the Wrangellia Composite Terrane (WCT) (Colpron et al., 2007; Martin-Short et al., 2018). Compared to the lower and higher frequency bands, the band between 0.5 and 2.0 Hz features significant development of Lg-wave energy (Figure 3b), and the Q_{Lg} values within this band are representative of the abovementioned five blocks (Figure 4g). Therefore, we calculated the logarithmic average of the Q_{Lg} values between 0.5 and 2.0 Hz to obtain a broadband Q_{Lg} model (Figure 3d). The broadband Q_{Lg} value spans a range from 10 to 600 in the Alaskan region. In this frequency band, the energy within the 3.7–2.9 km/s group velocity window primarily originates from Lg waves rather than from low-frequency surface waves (Figure 2b). This technique reduces the influence of surface waves on the measurement of Lg-wave amplitudes. Higher Q_{Lg} values were observed beneath the Brooks Range and the western WCT. The crust under the Canadian Cordillera in the east features high Q_{Lg} values (>400), while the crust beneath the ODT in western Alaska, the Aleutian volcanic arc, the BJV and the WVF in southern Alaska exhibits low Q_{Lg} (<200) values. The DVG had a slightly greater Q_{Lg} than the surrounding volcanic regions. Previous Lg-wave attenuation models also revealed similar low-Q_{Lg} zones beneath the WVF and arc volcanoes, as well as high-Q_{Lg} crust under the Brooks Range and the Canadian Cordillera (Hearn, 2021; Mahanama & Cramer, 2023), corresponding well to our broadband attenuation distributions. Low heat flow (<60 mW/m^2) was speculated to occur in the AAT, and high heat flow (>90 mW/m^2) was speculated to occur in south-central Alaska (Batir et al., 2016), correlating with the attenuation results over a broad area.

The uncertainty in the results can be affected by the ray coverage, data processing method, inversion system, etc., and is difficult to quantify. The bootstrapping technique (Efron, 1983) was used to investigate the stability. We randomly selected 80% of the raypaths from all single- and two-station data to form a partial data set and used it in the inversion. We repeated this process 100 times, followed by statistical analysis of these partial. Based on the comparison of Figure 5a with Figures 3b and 5c with Figure 3d, the mean Q_{Lg} map is consistent with the result inverted using the full data set. The spatial distribution of the standard deviation is shown in Figures 5b and 5d. In most areas, the standard deviations are significantly smaller than their mean values, validating the robustness of the data control and inversion system. Larger uncertainties mostly exist at the periphery with sparse ray coverage (refer to Figure S9 in Supporting Information S1). In addition, the broadband attenuation model has a smaller uncertainty (SD < 25) than that from a single frequency (SD < 60), indicating that averaging over frequencies can increase stability.

4. Discussion

4.1. Comparison Between the Crustal Attenuation Model and Existing Attenuation and Velocity Models

Previous researchers have conducted seismic attenuation studies in this region (Hearn, 2021; Mahanama & Cramer, 2023; McNamara, 2000; McSweeney et al., 1991; Soto Castaneda et al., 2021; Stachnik et al., 2004). The 2-D attenuation model beneath the YT shows two strong attenuation (low Q) zones in the mantle wedge, including

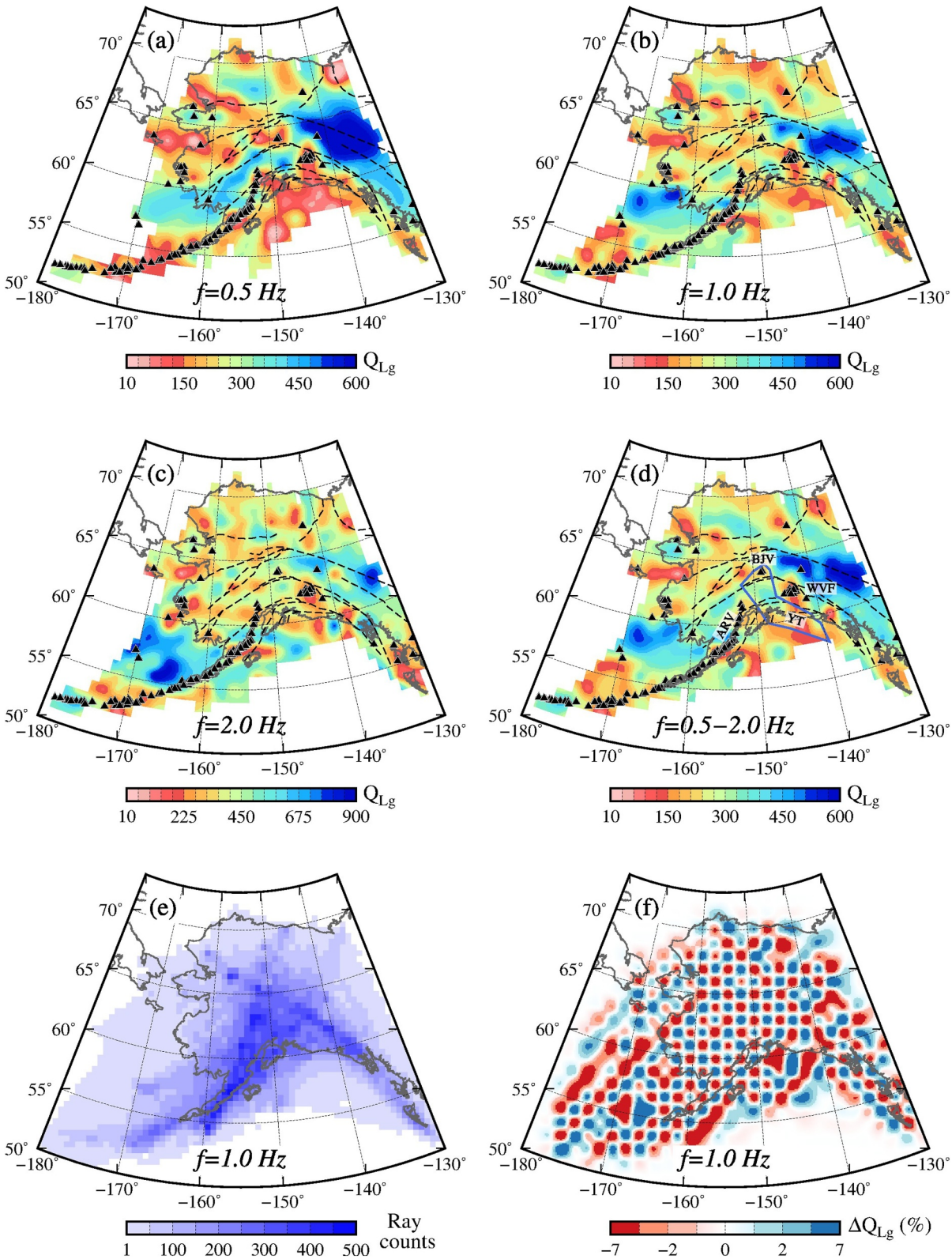

Figure 3.

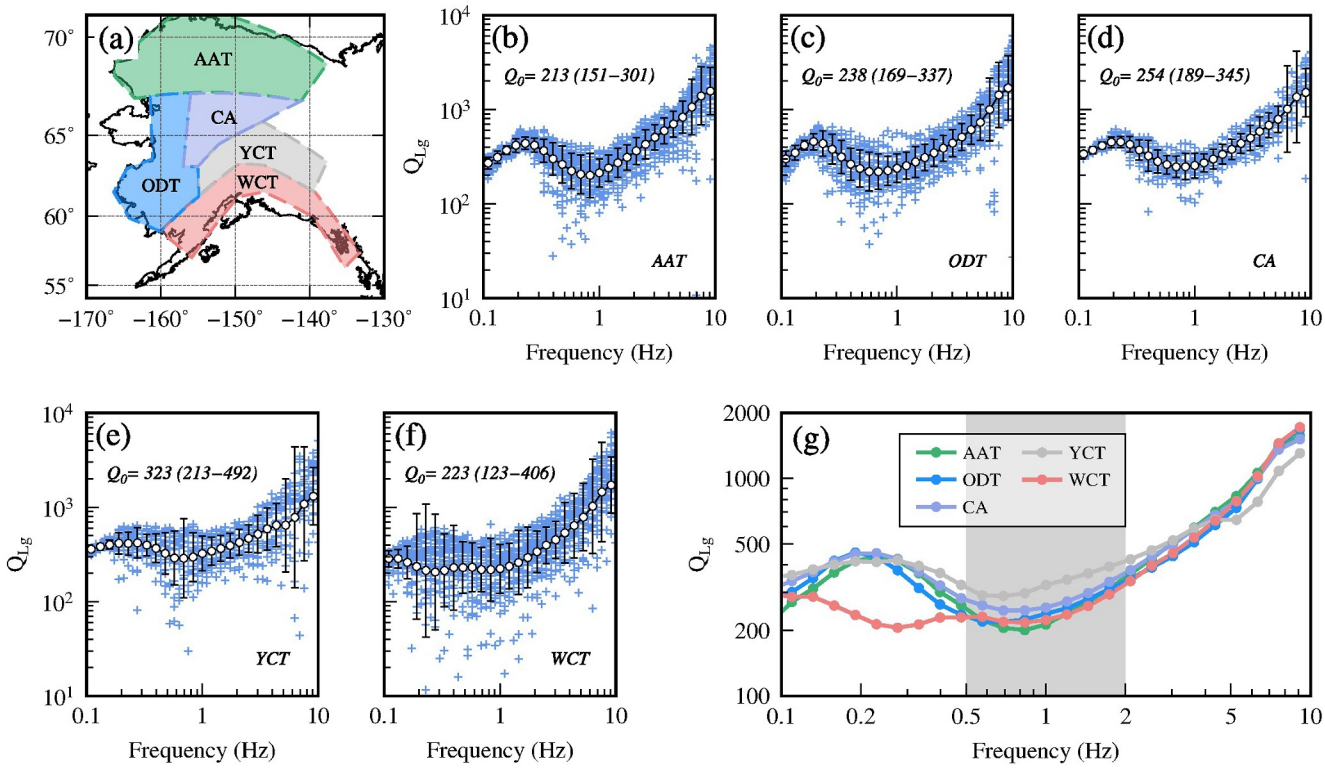

Figure 4. Frequency-dependent Q_{Lg} for selected blocks. (a) Map showing the boundaries of composite terranes in Alaska (Colpron et al., 2007; Martin-Short et al., 2018), including the Arctic Alaska Terrane (AAT), the Ocean Domain Terranes (ODT), Central Alaska (CA), the Yukon Composite Terrane (YCT) and the Wrangellia Composite Terrane (WCT). (b–f) Inverted Q_{Lg} values versus the frequency (blue crosses) for individual blocks, along with their mean values within narrow frequency bands (open circles) and logarithmic standard deviations (error bars). The Q_{Lg} at 1.0 Hz (Q_0) are labeled in each panel. (g) Comparison of Q_{Lg}-frequency curves for different blocks, in which attenuations in the shaded band between 0.5 and 2.0 Hz are selected to calculate a broadband Q_{Lg}.

a hot convecting mantle and an area of dehydration in the Yakutat crust (Stachnik et al., 2004). Teleseismic body-wave attenuation also revealed a hot mantle wedge and cold forearc in the Yakutat subduction system (Soto Castaneda et al., 2021). McNamara (2000) developed a frequency-dependent power law model for Lg-waves in south-central Alaska: $Q(f) = 220(\pm30)f^{0.66(\pm0.09)}$, where $Q_0 = 220(\pm30)$ is consistent with the Q_0 value in the WCT (Figure 4f). Hearn (2021) conducted Lg-wave attenuation tomography for the Alaskan mainland and identified a strong attenuation zone beneath the WVF, which is consistent with our attenuation model. Previous Lg-wave attenuation models also revealed similar high-Q_{Lg} crust under the Brooks Range and the Canadian Cordillera regions (Hearn, 2021; Mahanama & Cramer, 2023).

The observed Lg-wave attenuation in this study includes both intrinsic attenuation and scattering attenuation (e.g., Shearer, 2009). Intrinsic attenuation can result from the partial melting and high-temperature properties of deep crust materials, and scattering attenuation can be a consequence of complex structures in the upper crust. However, distinguishing between the two attenuation mechanisms based on the methods used and limited observations is difficult. In addition, many factors affect Lg-wave attenuation. For example, high Lg attenuation may be caused by water-rich layers in southern Tibet (Xie et al., 2004) and may be produced by sedimentary basins in the eastern US (Mitchell & Hwang, 1987). Therefore, we combine the observed strong apparent Lg attenuation with other geophysical anomalies, including low seismic velocities and high heat flow, to constrain

Figure 3. Crustal Lg-wave attenuation model of the Alaskan mainland. (a–c) Selected crustal Q_{Lg} images at 0.5, 1.0, and 2.0 Hz, respectively. The dashed black lines represent the major fault systems. The black triangles denote volcanoes. Q_{Lg} images at 3.0 and 5.0 Hz are shown in Figure S11 in Supporting Information S1. (d) Broadband Q_{Lg} images between 0.5 and 2.0 Hz. ARV: Aleutian arc volcanoes; BJV: Buzzard Creek-Jumbo Dome volcanoes; WVF: Wrangell Volcanic Field; YT: Yakutat Terrane. (e) 1.0 Hz ray density distribution, counts per 50 × 50 *km* element. The raypath distribution is shown in Figure S12 in Supporting Information S1. (f) 1° × 1° checkerboard resolution test at 1.0 Hz. Please refer to Figures S9 and S10 in Supporting Information S1 for more checkerboard tests with different input amplitudes.

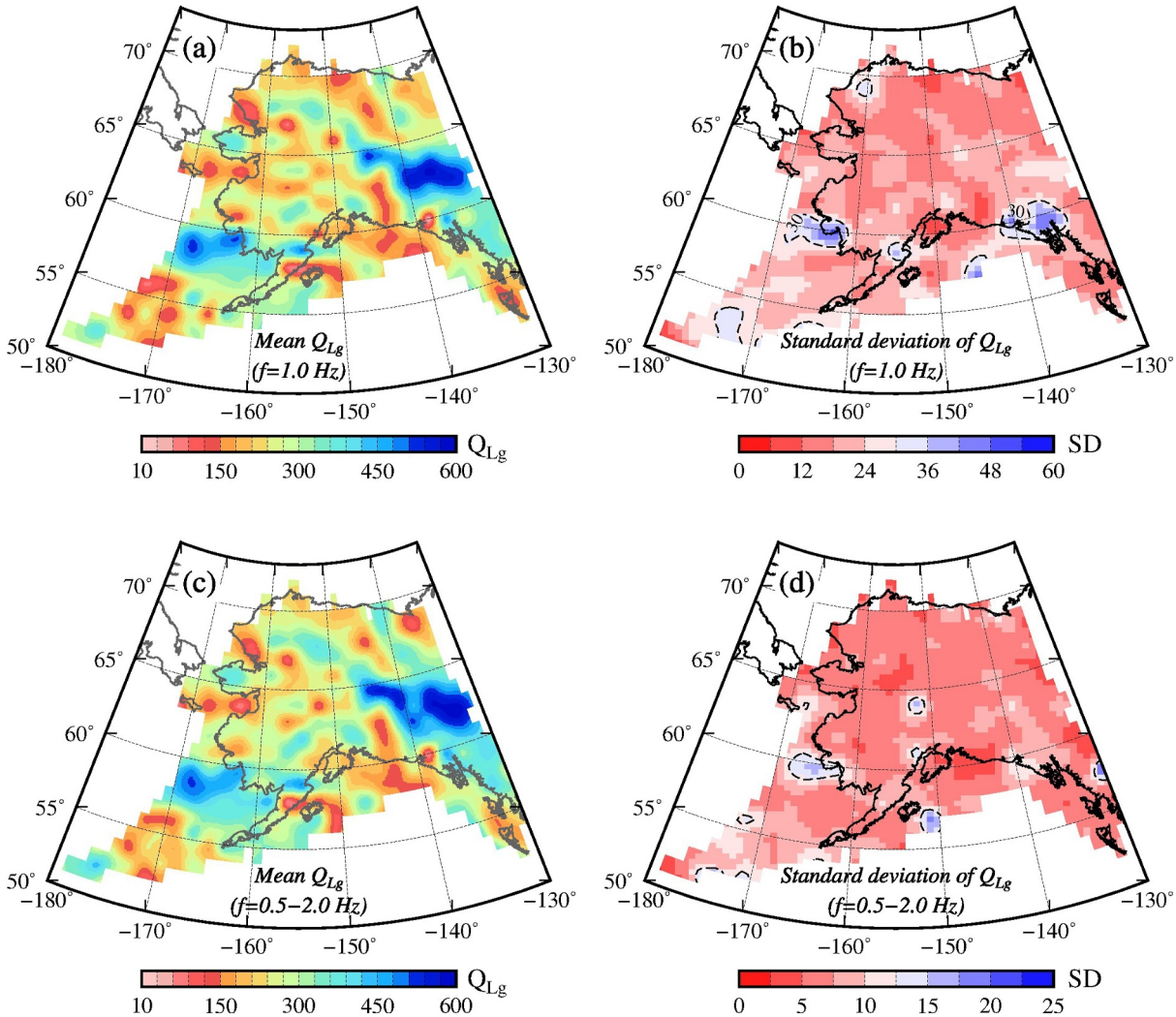

Figure 5. (a, c) The mean values of the 1.0 Hz and broadband (0.5–2.0 Hz) Q_{Lg} maps, respectively, obtained from the bootstrapping technique. (b, d) The standard deviations of the 1.0 Hz and broadband Q_{Lg} maps, respectively.

the distribution and location of high temperatures. The lateral variation in crustal Lg-wave attenuation is consistent with previous P- and S-wave velocity models (e.g., Berg et al., 2020; Feng et al., 2020; Jiang et al., 2018; Nayak et al., 2020; Ward & Lin, 2018). Combining attenuation and velocity information can significantly improve the understanding of subsurface thermodynamics. In south-central Alaska, three low-Q_{Lg} anomalies are revealed beneath the Aleutian arc volcanoes, the BJV and the WVF (Figure 3d). In the upper crust (~10 km depth), the P- and S-wave velocity models revealed low-velocity zones beneath the BJV and the WVF (Figures S13 and S14 in Supporting Information S1). They correspond to strong Lg-wave attenuation zones in these regions. The crust beneath the central YT is characterized by high-Q_{Lg} and high-velocity features. The cold YT with high Q_{Lg} values approximately terminates on the west side of the WVF. There are also some differences in the DVG between the velocity and attenuation results. The Lg-wave attenuation model revealed a relatively weak attenuation zone corresponding to the inactive volcanic region, where the velocity features in the upper crust remain controversial. In the middle and lower crust (~25 km depth), most of the P- and S-wave velocity models are consistent with each other (Figures S15 and S16 in Supporting Information S1). Extensive low-velocity anomalies beneath the WVF correspond to a strong Lg-wave attenuation zone. The central YT is characterized by high velocities. Note that the Lg-waves sample the whole crust. Accordingly, the Q_{Lg} results are for the entire crust, without sufficient depth resolution. Therefore, combining depth-dependent velocity structures can help

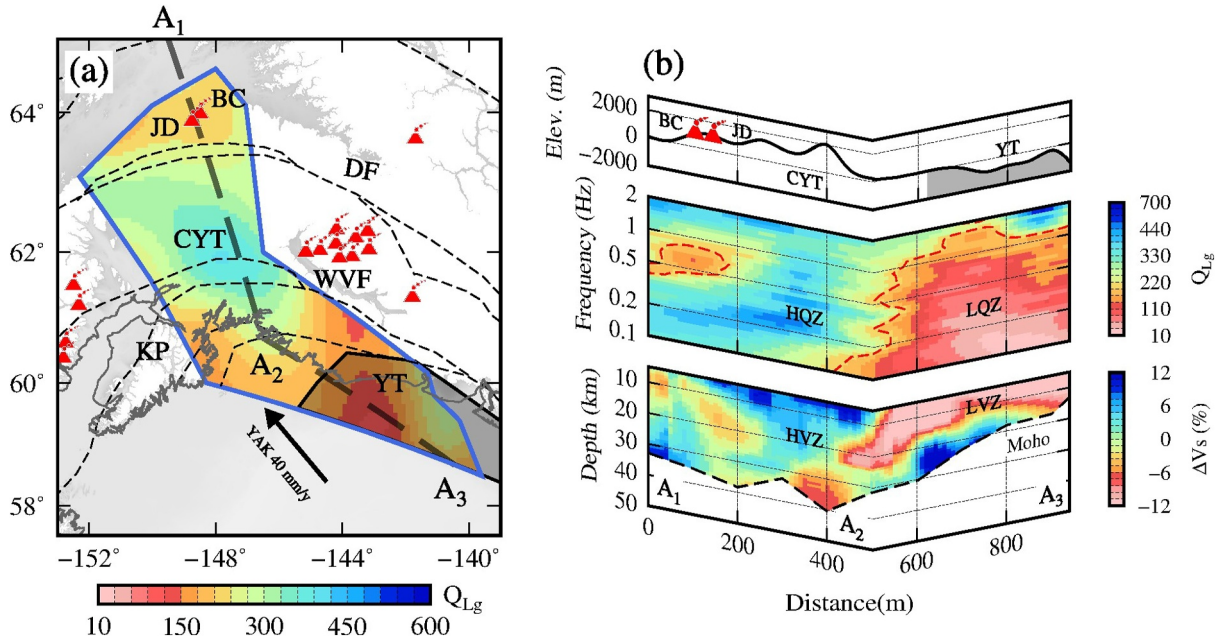

Figure 6. Crustal attenuation structure in the Yakutat terrane (YT). (a) Broadband Lg-wave attenuation model of the YT. The Yakutat microplate is bounded by the blue polygon, and the unsubducted part is marked by shading and is outlined with a black line (Eberhart-Phillips et al., 2006). (b) Cross-sections comparing different observations, with the surface traces marked by the thick dashed polyline A_1–A_2–A_3 in (a). (top) The surface topography and volcanic activity. (middle) Q_{Lg} versus frequency. The contours with Q_{Lg} = 200 are marked as red dashed lines. (bottom) Shear-wave velocity profiles (Berg et al., 2020). The Moho discontinuity was extracted from the CRUST1.0 model (Figure S17 in Supporting Information S1) (Laske et al., 2013). The vertical axis of the attenuation cross-section is frequency rather than depth. CYT: central Yakutat terrane, HQZ: high-Q_{Lg} zone, LQZ: low-Q_{Lg} zone, HVZ: high-velocity zone, LVZ: low-velocity zone.

locate the origins of attenuation anomalies. On the other hand, the close correlation between strong Lg-wave attenuation and volcanism ensures a tighter constraint on the spatial variation in thermal features than on the spatial variation in velocity distributions.

4.2. Crustal Thermal Structure in the Yakutat Terrane

The Yakutat region in southern Alaska has a corner-shaped tectonic structure at the end of the subducting Pacific plate and is adjacent to strike-slip faults to the east. The entire Yakutat microplate, or terrane, includes both the subducted and unsubducted parts (Eberhart-Phillips et al., 2006; Worthington et al., 2012). As shown in Figure 6a, the Yakutat microplate subducted beneath south-central Alaska at a shallow angle from the early Oligocene to the middle Miocene, and its northern boundary approximately reaches the Buzzard Creek region (Eberhart-Phillips et al., 2006; Finzel et al., 2011). The southeastern unsubducted YT (shadow zone in Figure 6a) is a region of over thickened oceanic crust that extends from 146°W to 137°W and is generally referred to as a young oceanic plateau (Bruhn et al., 2004; Christeson et al., 2010; Pavlis et al., 2004; Plafker et al., 1994). According to the crustal Lg attenuation model, the unsubducted YT and the overlying crust above the underthrusting Yakutat microplate exhibit completely different attenuation structures. As illustrated in Figure 6b, the offshore YT shows an extensive low-Q_{Lg} anomaly over a wide frequency range, which is consistent with low velocities in the crust (Berg et al., 2020). Note that the vertical axis of the attenuation cross-section is frequency rather than depth. The crystalline crustal thickness of offshore Yakutat ranges from ∼15 to ∼30 km based on seismic reflection and refraction profiles (e.g., Christeson et al., 2010; Worthington et al., 2012). It is reasonable to conclude that the propagation efficiency of Lg-waves is poorer in thick oceanic crust than in continental crust. According to seismic tomography and receiver function images, the subducted Yakutat crust features a LVZ ∼15–20 km thick below the Alaska range. The overlying crust above the subducted Yakutat microplate exhibits relatively weak attenuation features over a wide frequency band, which also aligns with high velocities in the crust (Figure 6b). Therefore, flat-slab subduction may have cooled the mantle wedge and inhibited the upwelling of hot mantle into the crust. Farther north, the Jumbo Dome-Buzzard Creek volcanoes developed above the northern edge of the

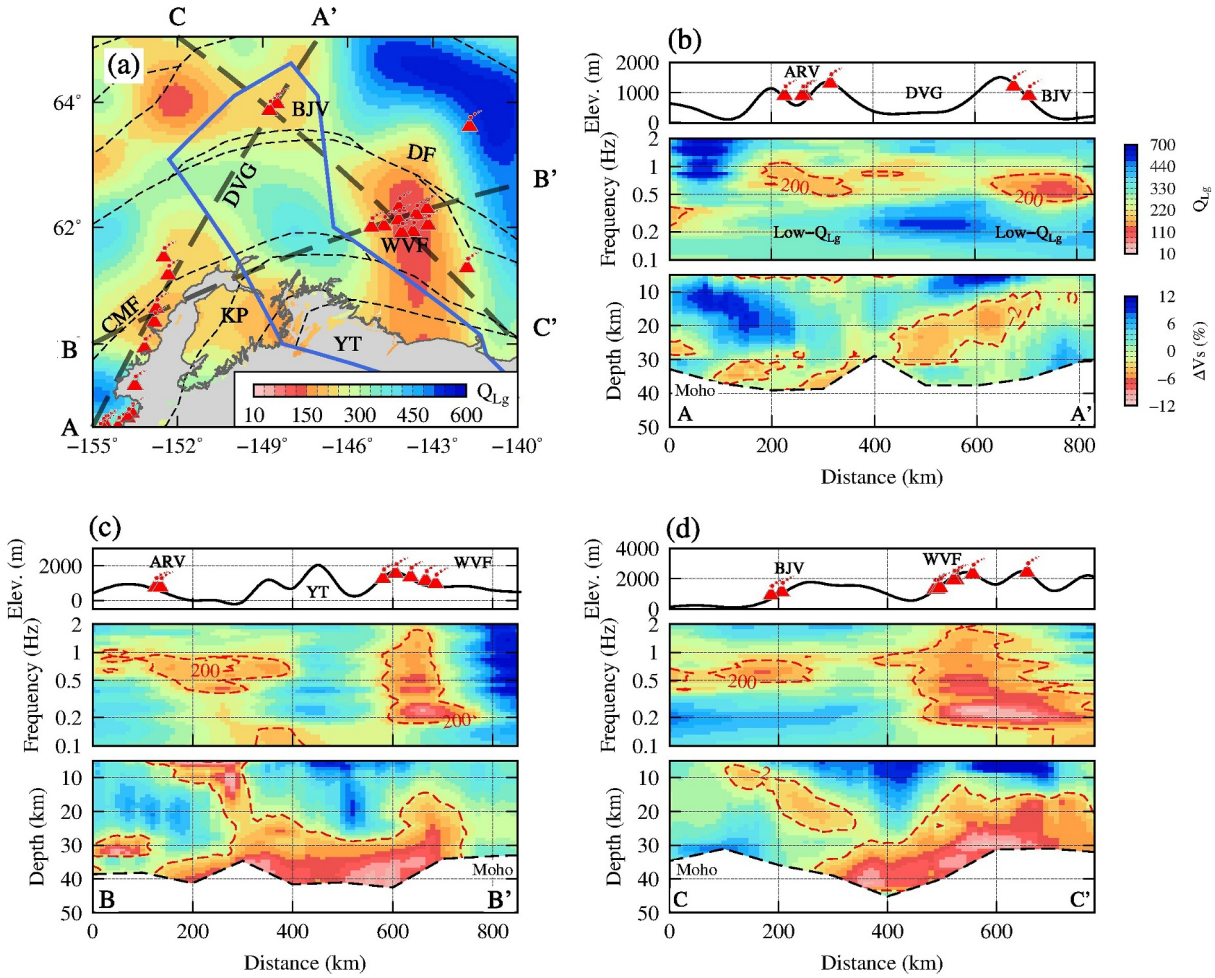

Figure 7. Comparison among frequency-dependent Q, seismic velocity and volcanic activity. (a) Broadband Lg-wave attenuation map of south-central Alaska. Three selected cross-sections are marked with thick dashed lines. (b–d) Cross-sections *A-A'*, *B-B'* and *C-C'* showing volcanic activity and surface topography (upper), Q_{Lg} versus frequency profiles (middle), and shear wave velocity profiles (bottom) (Berg et al., 2020). The vertical axis of the attenuation cross-section is frequency rather than depth. The contours with $Q_{Lg} = 200$ and $\Delta V_S = -2\%$ are marked as red dashed lines. The Moho discontinuity in the velocity cross-sections is from the CRUST1.0 model (Laske et al., 2013).

Yakutat plate, where the crust shows low-Q_{Lg} anomalies. The cooling of the mantle wedge caused by the Yakutat plate may terminate near the Jumbo Dome-Buzzard Creek region.

4.3. Is There Crustal Melt Beneath the Denali Volcanic Gap?

In south-central Alaska, the areas featuring strong Lg-wave attenuation are fully consistent with the volcanic activity surrounding the YT (Figure 7), indicating potential magma chambers in the crust. Figures 7b–7d compare cross-sections of Q_{Lg} versus frequency and velocity versus depth (Berg et al., 2020) through volcanic areas, with the surface traces shown as dashed lines in Figure 7a. Both cross-sections *A-A'* and *B-B'* reveal large volumes of accumulated crustal melt corresponding to low Q_{Lg} values and low velocities beneath the Aleutian arc volcanoes on the western side of the Yakutat microplate. Aleutian arc volcanism is generally attributed to Pacific subduction (Nakamura et al., 1977). Along cross-section *B-B'*, deeper low-velocity melts feed the crust, corresponding to strong attenuation at lower frequencies. This finding suggests that arc magmatism originates from the deep mantle. Compared with the Aleutian and Wrangell volcanoes, the BJV has a smaller scale (Figure 7d). As illustrated in Figure 8, high-resolution P-wave velocity tomography constrains the patterns of the subducting Pacific, Yakutat, and Wrangell slabs (Gou et al., 2019). The BJV has developed

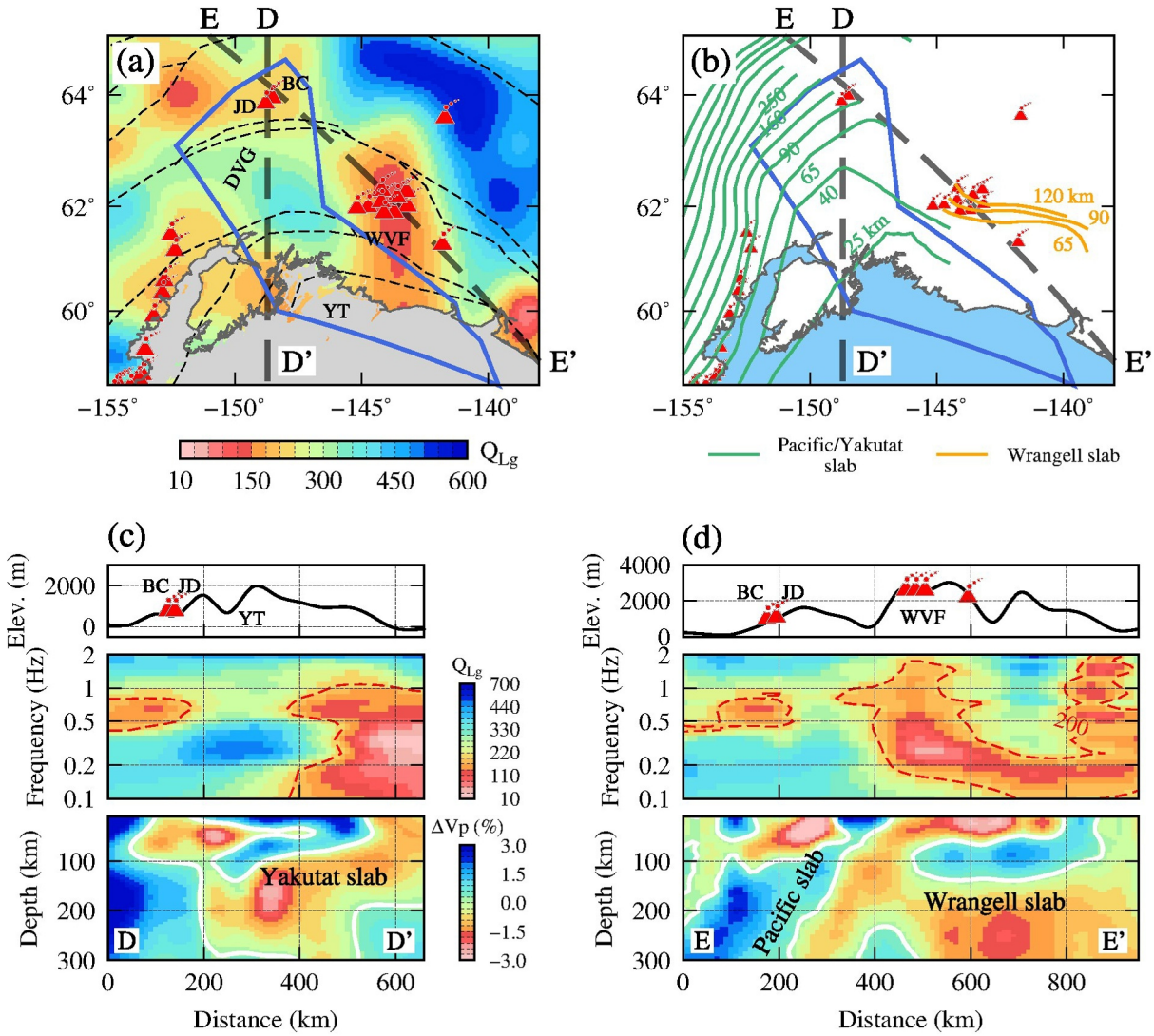

Figure 8. Comparison between the Lg-wave attenuation and P-wave velocity. (a) Attenuation map. Thick dashed lines mark surface traces of two selected cross-sections, *D-D'* and *E-E'*. (b) Depth contours of the subducted Pacific/Yakutat and Wrangell slabs based on the Wadati–Benioff zone seismicity and P-wave velocity tomography (modified from Gou et al., 2019). (c–d) Cross-sections *D-D'* and *E-E'*. (top) Surface topography and volcanism, (middle) Q_{Lg} versus frequency, and (bottom) P-wave velocity profiles (Gou et al., 2019). The vertical axis of the attenuation cross-section is frequency rather than depth.

above the northeastern edge of the Yakutat microplate, where the plate has subducted to ~100 km deep (Figure 8c). Therefore, it is possible that the crustal melts beneath the BJV originated from mantle upwelling in front of the Yakutat slab.

Between the BJV and Aleutian volcanic arc, the absence of magmatism is usually attributed to cooling caused by the flat-slab subduction of the Yakutat microplate. However, whether melt exists beneath the DVG is under ongoing debate. Some velocity tomography studies have revealed a fast mantle wedge beneath the DVG (Jiang et al., 2018; Liang et al., 2024; Ward & Lin, 2018; Yang & Gao, 2020), but other observations have suggested a low-velocity mantle wedge beneath the DVG (Feng & Ritzwoller, 2019; Gou et al., 2019; Martin-Short et al., 2018). A recent tomographic study also defined a crustal LVZ as a subduction-related crustal magma reservoir beneath the DVG (Rabade et al., 2023). According to the attenuation model, the crust beneath the DVG exhibits average or somewhat weak attenuation, in contrast with the apparent low Q_{Lg} values beneath the Aleutian volcanic arc to the west and the adjacent BJV to the east (Figure 7a). As shown in the cross-section *A-A'*, somewhat low Q_{Lg} values appear between 0.5 and 1.0 Hz beneath the DVG, but these

values are not as low as those beneath the volcanic areas (Figure 7b). The above observations suggest that, below the DVG, it is unlikely that large amounts of molten materials have accumulated in the crust and feed surface volcanoes.

4.4. Quarter-Toroidal Crustal Melting Beneath the WVF and BJV

The WVF has developed on the eastern edge of the YT and consists of 11 major volcanic centers with ages ranging from ~26 to ~0.2 Ma (Richter et al., 1990; Trop et al., 2012). Among all the volcanic zones, the WVF shows the strongest low-Q_{Lg} anomaly ($Q_{Lg} < 100$) (Figure 7a). As illustrated in cross-section *C*-*C*' in Figure 7d, the low-Q_{Lg} anomaly beneath the WVF spans a wide frequency range between 0.2 and 2.0 Hz, corresponding to a massive low-velocity shear-wave anomaly in the middle-lower crust. Based on crustal velocity reduction, Yang and Gao (2020) proposed that the WVF was supplied by a large crustal magma reservoir composed of rocks with 4%–6% partial melting. Several models have been proposed to explain the origin of the WVF. First, the adakitic signature suggests potential edge melting of the Yakutat slab, explaining the Wrangell volcanism there (Preece & Hart, 2004). Second, toroidal mantle flow around the Yakutat slab may lead to magma upwelling beneath the WVF, as suggested by seismic anisotropy observations (Christensen & Abers, 2010; Feng et al., 2020; Hanna & Long, 2012; McPherson et al., 2020; Venereau et al., 2019) and geodynamic modeling (Jadamec & Billen, 2010, 2012). Third, the subduction of the Wrangell slab or small-scale slab segments (Figure 8d) may have caused clustered volcanism, as supported by high seismic velocities (Boyce et al., 2023; Estève et al., 2020, 2021; Jiang et al., 2018; Yang & Gao, 2020), Wadati–Benioff seismicity (Daly et al., 2021; Stephens et al., 1984), receiver function images (Mann et al., 2022) and seismic attenuation (Soto Castaneda et al., 2021). A slab gap or tear may also provide a magmatic channel contributing to the Wrangell volcanism (Gou et al., 2019; Mann et al., 2022).

Strong attenuation is not solely limited to the crust beneath the WVF and BJV. Within the wide frequency band (0.5 and 2.0 Hz), a N–S-trending low-Q_{Lg} belt crosses the WVF and continues to extend northward (Figure 9a). In the northern YT, another low-Q_{Lg} anomaly extends westward from the BJV. These two low-Q_{Lg} belts are connected by a slightly weaker low-Q_{Lg} area ($240 \leq Q_{Lg} \leq 300$). To ensure the validity and resolution of this attenuation pattern, we conducted a synthetic test. We created three slightly different synthetic models as inputs: Figure 9c features two fully isolated low-Q_{Lg} anomalies beneath the two volcanic areas, Figure 9d features two connected low-Q_{Lg} anomalies, and Figure 9e features two weakly connected low-Q_{Lg} anomalies. The regional average Q_{Lg} is used as the background. The attenuation anomalies were set to ±10% perturbations, and ±5% random noise was added to the synthetic data set. The results show that the inversion system can distinguish these three cases well. Furthermore, the weakly connected zone with Q_{Lg} values slightly greater than those of the adjacent low-Q_{Lg} anomalies is clearly revealed (Figure 9h), which is consistent with the results from the real data (Figure 9a). Therefore, our tomographic results can be trusted, and crustal melts likely extend around the YT.

The curved crustal melt zone beneath the BJV and WVF may be related to the potential toroidal mantle flow suggested by seismic anisotropy (e.g., Christensen & Abers, 2010; Feng et al., 2020; Hanna & Long, 2012; Venereau et al., 2019). As shown in Figure 9b, previous shear-wave splitting analyses revealed a fast rotational direction around the edge of the Yakutat slab and suggested entrained flow beneath the Yakutat slab, toroidal flow around the slab edge, and slab-parallel flow in the mantle wedge (Venereau et al., 2019). Feng et al. (2020) also observed rotational shear-wave fast-velocity directions related to the slab geometry. In the upper crust, the fast-velocity direction is nearly parallel to the orientation of major faults (Feng et al., 2020). In the middle-lower crust, the P-wave fast-velocity directions also exhibit rotational patterns around the eastern and northern edges of the Yakutat microplate (Gou et al., 2019). As illustrated in Figure 9a, the fast-velocity direction roughly follows an N–S trend in the WVF low-Q_{Lg} belt and roughly changes to an E–W trend near the BJV to follow the low-Q_{Lg} region. Additionally, GPS measurements have revealed the counterclockwise movement of south-central Alaska (green arrows in Figure 9a) (Cross & Freymueller, 2008; Kreemer et al., 2014). Therefore, the crustal attenuation and seismic anisotropy observations in south-central Alaska both suggest the existence of a quarter-toroidal crustal melt channel that weakly connects the magmatic reservoirs under the WVF and BJV (Figure 10). This curved zone of crustal melting may be related to the thermal materials carried by toroidal flow in the mantle wedge.

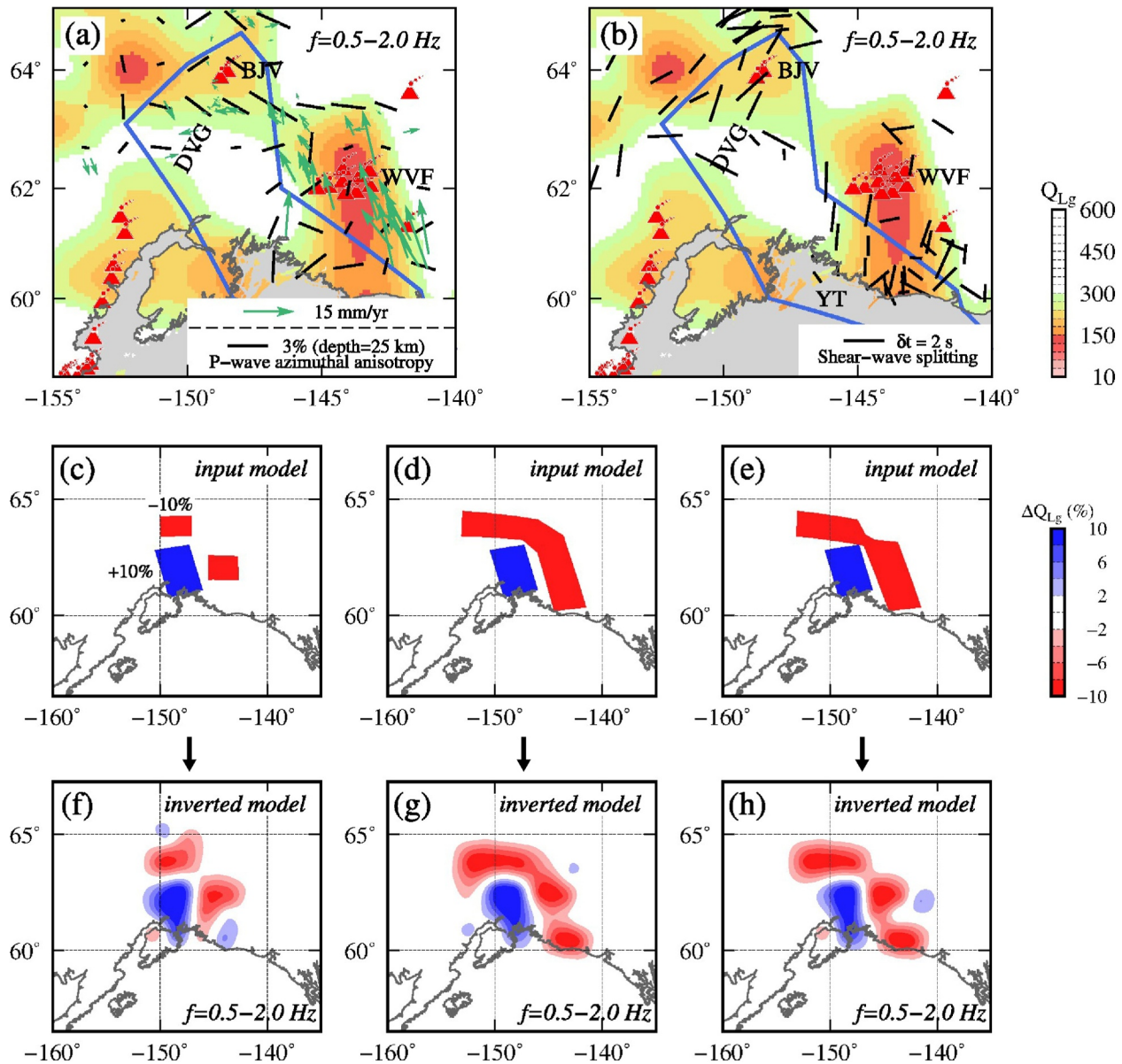

Figure 9. Quarter-toroidal crustal melting inferred from a curved low-Q_{Lg} belt. (a) Comparisons among crustal low-Q_{Lg} anomalies (0.5–2.0 Hz), P-wave azimuthal anisotropy in the crust (black lines) (Gou et al., 2019), and GPS velocities (green arrows) (Kreemer et al., 2014). (b) Previous shear-wave splitting observations (Venereau et al., 2019). (c–h) Resolution tests with synthetic models. Three synthetic attenuation models were used as input. In these models, two low-Q_{Lg} anomalies are (c) fully isolated, (d) tightly connected, and (e) weakly connected. The regional average Q_{Lg} is set as the background. The attenuation anomalies have ±10% perturbations, and 5% rms random noise is added to the synthetic data. Inverted attenuation images from three synthetic models are shown in figures f–h.

5. Conclusion

A high-resolution broadband Lg-wave attenuation model is constructed for the Alaskan mainland. The model reveals that the Brooks Range in northern Alaska and the Canadian Cordillera feature stable crust with weak attenuation. In south-central Alaska, the crust overlying the subducted Yakutat microplate shows relatively weak attenuation, indicating that flat-slab subduction may have cooled the mantle wedge and prevented hot mantle material from entering the crust (Figure 10). Apparent low-Q_{Lg} anomalies are observed beneath the Aleutian arc volcanoes, the BJV and the WVF. In contrast to the crust in these low-Q_{Lg} areas, the crust beneath the DVG features average or slightly weaker attenuation. Therefore, large amounts of melts are unlikely to have accumulated there to support surface volcanism. The curved low-Q_{Lg} belt in south-central Alaska represents a potential crustal melt channel with a quarter-toroidal pattern connecting the magmatic chambers under the WVF and

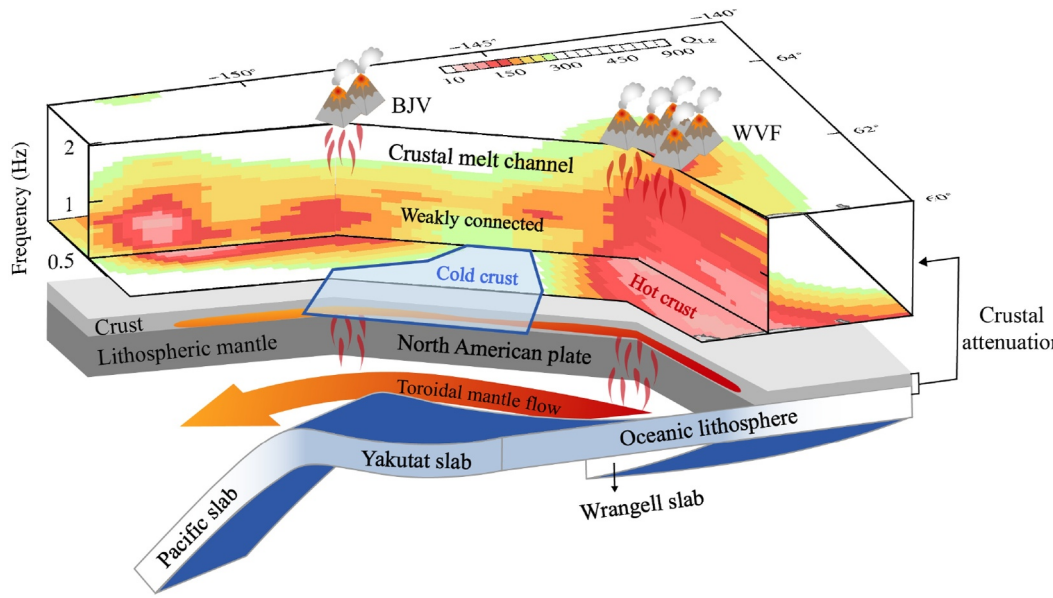

Figure 10. Schematic diagram of the quarter-toroidal crustal melt channel beneath south-central Alaska. The subduction patterns of the Yakutat and Wrangell slabs are constrained by seismic velocity tomography (Gou et al., 2019) (Figures S18 and S19 in Supporting Information S1) and receiver function imaging (Mann et al., 2022). The occurrence of toroidal flow in the mantle wedge is inferred based on seismic anisotropy observations (Christensen & Abers, 2010; Feng et al., 2020; Hanna & Long, 2012; Venereau et al., 2019) and geodynamic modeling (Jadamec & Billen, 2010). Note that we show the frequency-attenuation cross-section rather than the depth cross-section.

BJV (Figure 10). This quarter-toroidal crustal melting may be related to the thermal materials carried by toroidal mantle flow in the mantle wedge.

Data Availability Statement

Supporting Information includes Figures S1–S19 and Tables S1–S3 in Supporting Information S1 and S2. The waveforms used in this study were collected from the Incorporated Research Institutions for Seismology Data Management Center. Tables S1–S3 in Supporting Information S2 list the detailed station and earthquake information used in this study. The single- and two-station Lg amplitude data used in this study and the resulting Lg-wave attenuation model for the Alaskan mainland are available at (Yang et al., 2024). Certain figures were generated using Generic Mapping Tools (Wessel et al., 2019).

Acknowledgments
The comments from Editor F. Niu, reviewer C. H. Cramer, and two anonymous reviewers are valuable and greatly improved this manuscript. This research was supported by the National Natural Science Foundation of China (U2139206, 42104055, 41974054, and 41974061), the China Postdoctoral Science Foundation (2024M751295) and the Postdoctoral Fellowship Program of CPSF (GZC20240638).

References

Abers, G. A. (2008). Orogenesis from subducting thick crust and evidence from Alaska. *Active tectonics and seismic potential of Alaska*, *179*, 337–349. https://doi.org/10.1029/179GM19

Batir, J. F., Blackwell, D. D., & Richards, M. C. (2016). Heat flow and temperature-depth curves throughout Alaska: Finding regions for future geothermal exploration. *Journal of Geophysics and Engineering*, *13*(3), 366–378. https://doi.org/10.1088/1742-2132/13/3/366

Berg, E. M., Lin, F. C., Allam, A., Schulte-Pelkum, V., Ward, K. M., & Shen, W. (2020). Shear velocity model of Alaska via joint inversion of Rayleigh wave ellipticity, phase velocities, and receiver functions across the Alaska Transportable Array. *Journal of Geophysical Research: Solid Earth*, *125*(2), e2019JB018582. https://doi.org/10.1029/2019jb018582

Boyce, A., Liddell, M. V., Pugh, S., Brown, J., McMurchie, E., Parsons, A., et al. (2023). A new P-wave tomographic model (CAP22) for North America: Implications for the subduction and cratonic metasomatic modification history of Western Canada and Alaska. *Journal of Geophysical Research: Solid Earth*, *128*(3), e2022JB025745. https://doi.org/10.1029/2022jb025745

Boyd, O. S., Jones, C. H., & Sheehan, A. F. (2004). Foundering lithosphere imaged beneath the southern Sierra Nevada, California, USA. *Science*, *305*(5684), 660–662. https://doi.org/10.1126/science.1099181

Brueseke, M. E., Benowitz, J. A., Trop, J. M., Davis, K. N., Berkelhammer, S. E., Layer, P. W., & Morter, B. K. (2019). The Alaska Wrangell arc: ~30 Ma of subduction-related magmatism along a still active arc-transform junction. *Terra Nova*, *31*(1), 59–66. https://doi.org/10.1111/ter.12369

Bruhn, R. L., Pavlis, T. L., Plafker, G., & Serpa, L. (2004). Deformation during terrane accretion in the Saint Elias orogen, Alaska. *Geological Society of America Bulletin*, *116*(7–8), 771–787. https://doi.org/10.1130/b25182.1

Cameron, C. E., & Crass, S. W. (2022). Geologic database of information on volcanoes in Alaska (GeoDIVA): Alaska division of geological & geophysical surveys digital data series. *20*. https://doi.org/10.14509/30901

Christensen, D. H., & Abers, G. A. (2010). Seismic anisotropy under central Alaska from SKS splitting observations. *Journal of Geophysical Research*, *115*(B4), B04315. https://doi.org/10.1029/2009jb006712

Christeson, G. L., Gulick, S. P., van Avendonk, H. J., Worthington, L. L., Reece, R. S., & Pavlis, T. L. (2010). The Yakutat terrane: Dramatic change in crustal thickness across the Transition fault, Alaska. *Geology*, *38*(10), 895–898. https://doi.org/10.1130/G31170.1

Chuang, L., Bostock, M., Wech, A., & Plourde, A. (2017). Plateau subduction, intraslab seismicity, and the Denali (Alaska) volcanic gap. *Geology*, *45*(7), 647–650. https://doi.org/10.1130/g38867.1

Colpron, M., Nelson, J. L., & Murphy, D. C. (2007). Northern Cordilleran terranes and their interactions through time. *Geological Society of America Today*, *17*(4), 4. https://doi.org/10.1130/gsat01704-5a.1

Cross, R. S., & Freymueller, J. T. (2008). Evidence for and implications of a Bering plate based on geodetic measurements from the Aleutians and western Alaska. *Journal of Geophysical Research*, *113*(B7), B07405. https://doi.org/10.1029/2007jb005136

Dalton, C. A., Ekström, G., & Dziewonski, A. M. (2009). Global seismological shear velocity and attenuation: A comparison with experimental observations. *Earth and Planetary Science Letters*, *284*(1–2), 65–75. https://doi.org/10.1016/j.epsl.2009.04.009

Daly, K. A., Abers, G. A., Mann, M. E., Roecker, S., & Christensen, D. H. (2021). Subduction of an oceanic plateau across southcentral Alaska: High-resolution seismicity. *Journal of Geophysical Research: Solid Earth*, *126*(11), e2021JB022809. https://doi.org/10.1029/2021jb022809

Davis, A. S., & Plafker, G. (1986). Eocene basalts from the Yakutat terrane: Evidence for the origin of an accreting terrane in southern Alaska. *Geology*, *14*(11), 963–966. https://doi.org/10.1130/0091-7613(1986)14<963:ebftyt>2.0.co;2

Debayle, E., Bodin, T., Durand, S., & Ricard, Y. (2020). Seismic evidence for partial melt below tectonic plates. *Nature*, *586*(7830), 555–559. https://doi.org/10.1038/s41586-020-2809-4

Eberhart-Phillips, D., Christensen, D. H., Brocher, T. M., Hansen, R., Ruppert, N. A., Haeussler, P. J., & Abers, G. A. (2006). Imaging the transition from Aleutian subduction to Yakutat collision in central Alaska, with local earthquakes and active source data. *Journal of Geophysical Research*, *111*(B11303), B11303. https://doi.org/10.1029/2005jb004240

Efron, B. (1983). Estimating the error rate of a prediction rule: Improvement on cross-validation. *Journal of the American Statistical Association*, *78*(382), 316–331. https://doi.org/10.1080/01621459.1983.10477973

Ekstrom, G., Nettles, M., & Dziewonski, A. M. (2012). The global CMT project 2004-2010: Centroid-moment tensors for 13,017 earthquakes. *Physics of the Earth and Planetary Interiors*, *200*, 1–9. https://doi.org/10.1016/j.pepi.2012.04.002

Elliott, J. L., Larsen, C. F., Freymueller, J. T., & Motyka, R. J. (2010). Tectonic block motion and glacial isostatic adjustment in southeast Alaska and adjacent Canada constrained by GPS measurements. *Journal of Geophysical Research: Solid Earth*, *115*(B9), B09407. https://doi.org/10.1029/2009jb007139

Estève, C., Audet, P., Schaeffer, A. J., Schutt, D., Aster, R. C., & Cubley, J. (2020). The upper mantle structure of Northwestern Canada from teleseismic body wave tomography. *Journal of Geophysical Research: Solid Earth*, *125*(2), e2019JB018837. https://doi.org/10.1029/2019jb018837

Estève, C., Gosselin, J. M., Audet, P., Schaeffer, A. J., Schutt, D. L., & Aster, R. C. (2021). Surface-wave tomography of the Northern Canadian Cordillera using earthquake Rayleigh wave group velocities. *Journal of Geophysical Research: Solid Earth*, *126*(8), e2021JB021960. https://doi.org/10.1029/2021jb021960

Feng, L., Liu, C., & Ritzwoller, M. H. (2020). Azimuthal anisotropy of the crust and uppermost mantle beneath Alaska. *Journal of Geophysical Research: Solid Earth*, *125*(12), e2020JB020076. https://doi.org/10.1029/2020jb020076

Feng, L., & Ritzwoller, M. H. (2019). A 3-D shear velocity model of the crust and uppermost mantle beneath Alaska including apparent radial anisotropy. *Journal of Geophysical Research: Solid Earth*, *125*, e2020JB020076. https://doi.org/10.1029/2020JB020076

Finzel, E. S., Trop, J. M., Ridgway, K. D., & Enkelmann, E. (2011). Upper plate proxies for flat-slab subduction processes in southern Alaska. *Earth and Planetary Science Letters*, *303*(3–4), 348–360. https://doi.org/10.1016/j.epsl.2011.01.014

Gou, T., Zhao, D., Huang, Z., & Wang, L. (2019). Aseismic deep slab and mantle flow beneath Alaska: Insight from anisotropic tomography. *Journal of Geophysical Research: Solid Earth*, *124*(2), 1700–1724. https://doi.org/10.1029/2018jb016639

Hanna, J., & Long, M. D. (2012). SKS splitting beneath Alaska: Regional variability and implications for subduction processes at a slab edge. *Tectonophysics*, *530–531*, 272–285. https://doi.org/10.1016/j.tecto.2012.01.003

Hayes, G. P., Moore, G. L., Portner, D. E., Hearne, M., Flamme, H., Furtney, M., & Smoczyk, G. M. (2018). Slab2, a comprehensive subduction zone geometry model. *Science*, *362*(6410), 58–61. https://doi.org/10.1126/science.aat4723

He, Y., & Lü, Y. (2021). Anisotropic Pn tomography of Alaska and adjacent regions. *Journal of Geophysical Research: Solid Earth*, *126*(11), e2021JB022220. https://doi.org/10.1029/2021jb022220

Hearn, T. M. (2021). Crustal attenuation from USArray ML amplitude tomography. *Geophysical Journal International*, *224*(1), 199–206. https://doi.org/10.1093/gji/ggaa445

Jadamec, M. A., & Billen, M. I. (2010). Reconciling surface plate motions with rapid three-dimensional mantle flow around a slab edge. *Nature*, *465*(7296), 338–341. https://doi.org/10.1038/nature09053

Jadamec, M. A., & Billen, M. I. (2012). The role of rheology and slab shape on rapid mantle flow: Three-dimensional numerical models of the Alaska slab edge. *Journal of Geophysical Research*, *117*(B2), B02304. https://doi.org/10.1029/2011jb008563

Jiang, C., Schmandt, B., Ward, K. M., Lin, F. C., & Worthington, L. L. (2018). Upper mantle seismic structure of Alaska from Rayleigh and S wave tomography. *Geophysical Research Letters*, *45*(19), 10350–10359. https://doi.org/10.1029/2018gl079406

Koehler, R. D. (2013). Quaternary faults and folds (QFF): Alaska division of geological & geophysical surveys digital data series. *3*. https://doi.org/10.14509/24956

Kreemer, C., Blewitt, G., & Klein, E. C. (2014). A geodetic plate motion and global strain rate model. *Geochemistry, Geophysics, Geosystems*, *15*(10), 3849–3889. https://doi.org/10.1002/2014gc005407

Laske, G., Masters, G., Ma, Z., & Pasyanos, M. (2013). Update on CRUST1.0 – A 1-degree global model of Earth's crust. In *EGU general assembly 2013*.

Leonard, L. J., Hyndman, R. D., Mazzotti, S., Nykolaishen, L., Schmidt, M., & Hippchen, S. (2007). Current deformation in the northern Canadian Cordillera inferred from GPS measurements. *Journal of Geophysical Research: Solid Earth*, *112*(B11), B11401. https://doi.org/10.1029/2007jb005061

Liang, X., Zhao, D., Hua, Y., & Xu, Y. G. (2024). Big mantle wedge and intraplate volcanism in Alaska: Insight from anisotropic tomography. *Journal of Geophysical Research: Solid Earth*, *129*(1), e2023JB027617. https://doi.org/10.1029/2023jb027617

Mahanama, A., & Cramer, C. H. (2023). Lateral variations of attenuation in the crust of Alaska using Lg Q tomography. *Bulletin of the Seismological Society of America*, *113*(3), 1054–1063. https://doi.org/10.1785/0120220164

Mann, M. E., Abers, G. A., Daly, K. A., & Christensen, D. H. (2022). Subduction of an oceanic plateau across Southcentral Alaska: Scattered-wave imaging. *Journal of Geophysical Research: Solid Earth*, *127*(1), e2021JB022697. https://doi.org/10.1029/2021jb022697

Martin-Short, R., Allen, R., Bastow, I. D., Porritt, R. W., & Miller, M. S. (2018). Seismic imaging of the Alaska subduction zone: Implications for slab geometry and volcanism. *Geochemistry, Geophysics, Geosystems*, *19*(11), 4541–4560. https://doi.org/10.1029/2018gc007962

McNamara, D. E. (2000). Frequency dependent Lg attenuation in south-central Alaska. *Geophysical Research Letters*, *27*(23), 3949–3952. https://doi.org/10.1029/2000gl011732

McPherson, A. M., Christensen, D. H., Abers, G. A., & Tape, C. (2020). Shear wave splitting and mantle flow beneath Alaska. *Journal of Geophysical Research: Solid Earth*, *125*(4), e2019JB018329. https://doi.org/10.1029/2019jb018329

McSweeney, T. J., Biswas, N. N., Mayeda, K., & Aki, K. (1991). Scattering and anelastic attenuation of seismic energy in central and south-central Alaska. *Physics of the Earth and Planetary Interiors*, *67*(1–2), 115–122. https://doi.org/10.1016/0031-9201(91)90065-p

Mitchell, B. J., & Hwang, H. J. (1987). Effect of low Q sediments and crustal Q on Lg attenuation in the United States. *Bulletin of the Seismological Society of America*, *77*(4), 1197–1210. https://doi.org/10.1785/BSSA0770041197

Nakamura, K., Jacob, K. H., & Davies, J. N. (1977). Volcanos as possible indicators of tectonic stress orientation-Aleutians and Alaska. *Pure and Applied Geophysics*, *115*(1–2), 87–112. https://doi.org/10.1007/bf01637099

Nayak, A., Eberhart-Phillips, D., Ruppert, N. A., Fang, H., Moore, M. M., Tape, C., et al. (2020). 3D seismic velocity models for Alaska from joint tomographic inversion of body-wave and surface-wave data. *Seismological Research Letters*, *91*(6), 3106–3119. https://doi.org/10.1785/0220200214

Ottemöller, L., Shapiro, N. M., Krishna Singh, S., & Pacheco, J. F. (2002). Lateral variation of Lg wave propagation in southern Mexico. *Journal of Geophysical Research*, *107*(B1). https://doi.org/10.1029/2001jb000206

Paige, C. C., & Saunders, M. A. (1982). Lsqr: An algorithm for sparse linear equations and sparse least squares. *ACM Transactions on Mathematical Software*, *8*(1), 43–71. https://doi.org/10.1145/355984.355989

Pasyanos, M. E., Matzel, E. M., Walter, W. R., & Rodgers, A. J. (2009). Broad-band Lg attenuation modelling in the Middle East. *Geophysical Journal International*, *177*(3), 1166–1176. https://doi.org/10.1111/j.1365-246X.2009.04128.x

Pavlis, T. L., Picornell, C., Serpa, L., Bruhn, R. L., & Plafker, G. (2004). Tectonic processes during oblique collision: Insights from the St. Elias orogen, northern North American Cordillera. *Tectonics*, *23*(3), TC3001. https://doi.org/10.1029/2003tc001557

Plafker, G., Moore, J. C., & Winkler, G. R. (1994). Geology of the southern Alaska margin. *Geology of the Southern Alaska Margin*.

Preece, S. J., & Hart, W. K. (2004). Geochemical variations in the <5 Ma Wrangell volcanic field, Alaska: Implications for the magmatic and tectonic development of a complex continental arc system. *Tectonophysics*, *392*(1–4), 165–191. https://doi.org/10.1016/j.tecto.2004.04.011

Rabade, S., Lin, F. C., Tape, C., Ward, K. M., Waldien, T., & Allam, A. (2023). The crustal magmatic structure beneath the Denali volcanic gap imaged by a dense linear seismic array. *Journal of Geophysical Research: Solid Earth*, *128*(12), e2023JB027152. https://doi.org/10.1029/2023jb027152

Richter, D. H., Smith, J. G., Lanphere, M. A., Dalrymple, G. B., Reed, B. L., & Shew, N. (1990). Age and progression of volcanism, Wrangell volcanic field, Alaska. *Bulletin of Volcanology*, *53*(1), 29–44. https://doi.org/10.1007/bf00680318

Ringdal, F., Marshall, P. D., & Alewine, R. W. (1992). Seismic yield determination of Soviet underground nuclear explosions at the Shagan River test site. *Geophysical Journal International*, *109*(1), 65–77. https://doi.org/10.1111/j.1365-246X.1992.tb00079.x

Sereno, T. J., Bratt, S. R., & Bache, T. C. (1988). Simultaneous inversion of regional wave spectra for attenuation and seismic moment in Scandinavia. *Journal of Geophysical Research*, *93*(B3), 2019–2035. https://doi.org/10.1029/JB093iB03p02019

Shearer, P. M. (2009). *Introduction to seismology* (2 ed.). Cambridge University Press.

Soto Castaneda, R. A., Abers, G. A., Eilon, Z. C., & Christensen, D. H. (2021). Teleseismic attenuation, temperature, and melt of the upper mantle in the Alaska subduction zone. *Journal of Geophysical Research: Solid Earth*, *126*(7). https://doi.org/10.1029/2021jb021653

Stachnik, J. C., Abers, G. A., & Christensen, D. H. (2004). Seismic attenuation and mantle wedge temperatures in the Alaska subduction zone. *Journal of Geophysical Research*, *109*(B10), B10304. https://doi.org/10.1029/2004jb003018

Stephens, C. D., Fogleman, K. A., Lahr, J. C., & Page, R. A. (1984). Wrangell-Benioff zone, southern Alaska. *Geology*, *12*(6), 373–376. https://doi.org/10.1130/0091-7613(1984)12<373:Wbzsa>2.0.Co;2

Street, R. L., Herrmann, R. B., & Nuttli, O. W. (1975). Spectral characteristics of the Lg wave generated by central United States earthquakes. *Geophysical Journal International*, *41*(1), 51–63. https://doi.org/10.1111/j.1365-246X.1975.tb05484.x

Trop, J. M., Hart, W. K., Snyder, D., & Idleman, B. (2012). Miocene basin development and volcanism along a strike-slip to flat-slab subduction transition: Stratigraphy, geochemistry, and geochronology of the central Wrangell volcanic belt, Yakutat-North America collision zone. *Geosphere*, *8*(4), 805–834. https://doi.org/10.1130/ges00762.1

Venereau, C. M. A., Martin-Short, R., Bastow, I. D., Allen, R. M., & Kounoudis, R. (2019). The role of variable slab dip in driving mantle flow at the eastern edge of the Alaskan subduction margin: Insights from shear-wave splitting. *Geochemistry, Geophysics, Geosystems*, *20*(5), 2433–2448. https://doi.org/10.1029/2018gc008170

Ward, K. M., & Lin, F. C. (2018). Lithospheric structure across the Alaskan Cordillera from the joint inversion of surface waves and receiver functions. *Journal of Geophysical Research: Solid Earth*, *123*(10), 8780–8797. https://doi.org/10.1029/2018jb015967

Wessel, P., Luis, J. F., Uieda, L., Scharroo, R., Wobbe, F., Smith, W. H. F., & Tian, D. (2019). The generic mapping tools version 6. *Geochemistry, Geophysics, Geosystems*, *20*(11), 5556–5564. https://doi.org/10.1029/2019gc008515

Wilson, F. H., Hults, C. P., Mull, C. G., & Karl, S. M. (2015). Geologic map of Alaska. *Geological Survey Scientific Investigations Map*, 196. https://doi.org/10.3133/sim3340

Worthington, L. L., Van Avendonk, H. J. A., Gulick, S. P. S., Christeson, G. L., & Pavlis, T. L. (2012). Crustal structure of the Yakutat terrane and the evolution of subduction and collision in southern Alaska. *Journal of Geophysical Research*, *117*(B1), B01102. https://doi.org/10.1029/2011jb008493

Xie, J., Gok, R., Ni, J., & Aoki, Y. (2004). Lateral variations of crustal seismic attenuation along the INDEPTH profiles in Tibet fromLg Qinversion. *Journal of Geophysical Research*, *109*(B10), B10308. https://doi.org/10.1029/2004jb002988

Xie, J. K. (1993). Simultaneous Inversion for source spectrum and path-Q using Lg with application to 3 Semipalatinsk explosions. *Bulletin of the Seismological Society of America*, *83*(5), 1547–1562. https://doi.org/10.1785/bssa0830051547

Yang, G., Chen, L., Zhao, L. F., Xie, X. B., & Yao, Z. X. (2023). Crustal Lg attenuation beneath the Iranian Plateau: Implications for Cenozoic magmatism related to slab subduction, slab break-off, and mantle flow. *Journal of Geophysical Research: Solid Earth*, *128*(3), e2022JB025664. https://doi.org/10.1029/2022JB025664

Yang, G., Zhao, L. F., Xie, X. B., He, X., Zhang, L., & Yao, Z. X. (2024). Strong Lg-wave attenuation reveals quarter-toroidal crustal melting around the Yakutat terrane in south-central Alaska [Dataset]. *World Data Center for Geophysics*. https://doi.org/10.12197/2023GA024

Yang, X., & Gao, H. (2020). Segmentation of the Aleutian-Alaska subduction zone revealed by full-wave ambient noise tomography: Implications for the along-strike variation of volcanism. *Journal of Geophysical Research: Solid Earth*, *125*(11), e2020JB019677. https://doi.org/10.1029/2020jb019677

Zhao, L. F., & Mousavi, S. M. (2018). Lateral variation of crustal Lg attenuation in eastern North America. *Scientific Reports*, *8*(1), 7285. https://doi.org/10.1038/s41598-018-25649-5

Zhao, L.-F., Xie, X.-B., Wang, W.-M., Zhang, J.-H., & Yao, Z.-X. (2010). Seismic Lg-wave Q tomography in and around Northeast China. *Journal of Geophysical Research*, *115*(B8), B08307. https://doi.org/10.1029/2009jb007157

Zhao, L.-F., Xie, X.-B., Wang, W.-M., Zhang, J.-H., & Yao, Z.-X. (2013). Crustal Lg attenuation within the North China craton and its surrounding regions. *Geophysical Journal International*, *195*(1), 513–531. https://doi.org/10.1093/gji/ggt235

References From the Supporting Information

Liu, M., & Gao, H. (2023). Variations of crustal thickness in Alaska and Northwestern Canada: Implications for crustal modification and accretion of tectonic units. *Journal of Geophysical Research: Solid Earth*, *128*(10), e2023JB027428. https://doi.org/10.1029/2023jb027428